



# Evaluation of chemical stability, thermal expansion coefficient, and electrical properties of solid state and wet-chemical synthesized Y and Mn-codoped $\text{CeO}_2$ for solid oxide fuel cells

Hala T. Handal <sup>a,b</sup>, Venkataraman Thangadurai <sup>a,\*</sup>

<sup>a</sup> Department of Chemistry, University of Calgary, 2500 University Dr NW, Calgary, AB, T2N 1N4 Canada

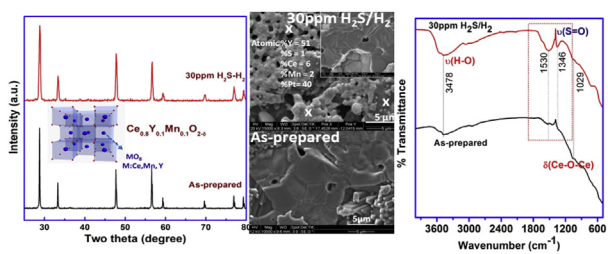
<sup>b</sup> Department of Inorganic Chemistry, National Research Centre, 12622 Dokki, Cairo, Egypt



## HIGHLIGHTS

- Co-doped ceria containing yttrium and manganese was prepared via ceramic and wet chemistry routes.
- DRS and IR were employed to study metal oxide segregation in doped ceria.
- Thermal expansion coefficient of ceria was determined using *in-situ* HT-XRD.
- CYMO at 300 °C under 30 ppm  $\text{H}_2\text{S} + \text{H}_2$  exhibits three orders of magnitude higher conductivity than in  $\text{H}_2$ .

## GRAPHICAL ABSTRACT



## ARTICLE INFO

### Article history:

Received 4 March 2013

Received in revised form

27 May 2013

Accepted 28 May 2013

Available online 10 June 2013

### Keywords:

Ceria solid solution  
Powder X-ray diffraction  
Electrical conductivity  
AC impedance  
Sulfur poisoning  
FTIR spectra

## ABSTRACT

Chemical stability and high electrical conductivity under the operating conditions of solid oxide fuel cell (SOFC) are considered as the momentum for innovating solid electrolytes and electrodes. In this paper, we report synthesis, structure, chemical stability and electrical conductivity of novel co-doped  $\text{Ce}_{0.9-x}\text{Y}_{0.1}\text{Mn}_x\text{O}_{2-\delta}$  ( $x = 0-15$  mol%) (CYMO). X-ray diffraction of Mn and Y-doped  $\text{CeO}_2$  shows the formation of fluorite-type structure with a space group  $Fm-3m$ . A few weak peaks corresponding to a tetragonal  $\text{Mn}_3\text{O}_4$  phase has been detected in some samples. Solubility of Mn in ceria is explained by considering the influence of the ionic radius, the crystal structure and its electronic structure. Thermal analysis shows dissimilarity between the reduction behavior of  $\text{Ce}_{0.9}\text{Mn}_{0.1}\text{O}_{2-\delta}$  and  $\text{Ce}_{0.9-x}\text{Y}_{0.1}\text{Mn}_x\text{O}_{2-\delta}$ .  $\text{Ce}_{0.8}\text{Y}_{0.1}\text{Mn}_{0.1}\text{O}_{2-\delta}$  exhibited the highest conductivity of  $\sim 6 \times 10^{-2} \text{ S cm}^{-1}$  and  $0.15 \text{ S cm}^{-1}$  at 700 °C in air and  $\text{H}_2$ , respectively. Surface studies have confirmed the formation of S species upon exposure to 30 ppm  $\text{H}_2\text{S}$  in  $\text{H}_2$  and a mechanism for S poisoning is presented.

© 2013 Elsevier B.V. All rights reserved.

## 1. Introduction

At present, solid oxide fuel cells (SOFCs) are drawing great interest because of their high efficiency, reliability, reducing environmental impact and tremendous potential for power generation.

Fuel flexibility and incorporation of non-precious catalysts make SOFCs dominate over proton exchange membrane fuel cells, phosphoric acid fuel cells, and alkaline fuel cells [1]. A typical high temperature SOFC electrolyte is 8 mol% Y-stabilized zirconia (YSZ) which exhibits high oxide ion conduction at 1000 °C, as well as redox stability under the low oxygen partial pressure ( $p\text{O}_2$ ) of the anode side [2]. However, the high temperature required for SOFC results in degradation problems over a long-term operation besides a relatively expensive manufacturing cost. Thus, it becomes

\* Corresponding author. Tel.: +1 403 210 8649; fax: +1 403 289 9488.  
E-mail address: [vthangad@ucalgary.ca](mailto:vthangad@ucalgary.ca) (V. Thangadurai).

mandatory to reduce the operating temperature of SOFC in order to widespread their commercialization.

For intermediate temperature (IT) SOFCs, acceptor-doped  $\text{Ce}_{1-x}\text{M}_x\text{O}_{2-\delta}$ , ( $\text{M}$  = trivalent rare earth ions) is considered as an alternative to YSZ since the ionic conductivity is about an order of magnitude higher than that of YSZ [3]. One of the major drawbacks of ceria is their partial reducibility under lower  $p\text{O}_2$ , where  $\text{Ce}^{4+}$  ion is being reduced to  $\text{Ce}^{3+}$  which could result in electronic current thorough the electrolyte and mechanical failure due to the severe expansion coefficient differences between air and reducing conditions. In addition, ceria requires high sintering temperature exceeding more than 1600 °C to prepare dense membrane, which results in grain coarsening and mechanical issues [4,5].

Recently, soft-chemical synthesis routes were employed to enhance the sinterability of ceria which are based on controlling the particle size as predicted by Herring's scaling law [6]. The most used synthetic techniques, including oxalate co-precipitation [7], sol–gel [8], Pechini process [9,10] and nitrate decomposition [11]. Of relevance to this conjuncture a recent research [12] had revealed thorough explanation for the effect of different particle size powders on the sintering behavior of  $\text{CeO}_2$ . Another approach to improve sinterability of doped  $\text{CeO}_2$  at lower temperatures is to introduce transition metal oxides (TMOs) to the fluorite lattice which proved to be very effective sintering aids for doped  $\text{CeO}_2$  [13–16]. Kilner and his co-workers [15] reported that the sintering temperature of commercial  $\text{CeO}_2$  could be reduced to 1300 °C by addition of 1 mol% Mn. However, this insertion leads to detrimental effect on the grain-boundary conductivity, and consequently, the total conductivity. Park and Yoo [17] explained the low solubility limit of Mn in Gd-doped  $\text{CeO}_2$  (GDC) which was found to be less than 1 mol% that it precipitated as manganese oxide at the grain-boundary. Thus, the goal of the present work is to investigate the effect of addition of manganese oxide on the physical and chemical properties of Y-doped  $\text{CeO}_2$  (CYO) and to check their functional physical and chemical properties for SOFCs.

## 2. Experimental section

### 2.1. Synthesis

A direct homogeneous co-precipitation synthesis was used to prepare powders of 10 mol% Y-doped  $\text{CeO}_2$  (CYO), 10 mol% Mn-doped  $\text{CeO}_2$  (CMO) and  $\text{Ce}_{0.9-x}\text{Y}_{0.1}\text{Mn}_x\text{O}_2$  (CYMO) ( $x = 5, 10$  and 15 mol%) [18]. Stoichiometric amounts of cerium nitrate (99.9%, Alfa Aesar), Y nitrate (99.9%, Alfa Aesar), and  $\text{MnCl}_2$  (99.9%, Fisher Scientific), were separately dissolved in bi-distilled water, mixed together and added to an appropriate amount of 1 M hexamethylenetetramine solution followed by stirring for 1 h at 80 °C. Then, the mixed solution was kept on stirring at room temperature for 24 h. Precipitate formed was filtered and washed with 2-propanol. The resultant powders were dried and then sintered in air at 1400 °C for 12 h with heating rate of 10 °C min<sup>-1</sup>. Doped  $\text{CeO}_2$  were also prepared by the solid-state (ceramic) reaction from high purity powders of  $\text{CeO}_2$  (99.9%, Alfa Aesar),  $\text{Y}_2\text{O}_3$  (99.9%, Alfa Aesar), and  $\text{MnCO}_3$  (99.9%, Aldrich). Stoichiometric amounts of metal oxides and salts were mixed by ball milling in 2-propanol for 6 h (Fritch Pulverisette-4 planetary mill). The samples were uniaxially – isostatically pressed into pellets and sintered at 1400 °C for 12 h. Commercial GDC (fuel cell materials) was used for comparison where it was pressed in to pellets and thermally treated at 1400 °C/5 h.

### 2.2. Phase analysis

Powder X-ray diffraction (PXRD) (Bruker D8 Advance powder X-ray diffractometer Cu K $\alpha$ , 40 kV, 40 mA; 2 $\theta$  range 10° to 80°) was

used to check phase formation. Lattice parameter was computed by least-squares refinement and the mean crystallite size was obtained using Debye–Scherrer's equation:

$$D = 0.9\lambda/(\beta\cos\theta) \quad (1)$$

where  $D$  is the crystallite size,  $\beta$  is the full width at half maximum (FWHM), and  $\lambda$  is the X-ray wavelength for  $\text{CuK}\alpha = 0.15418$  nm. The theoretical density of the formed solid solutions can be calculated according to the Equation (2) [19]:

$$\rho_{\text{th}} = 4/(N_A V)[(1 - x)M_{\text{Ce}} + xM_{\text{Y}} + (2 - 0.5x)M_{\text{O}}] \quad (2)$$

where,  $x$  is Y content,  $V$  is the volume of the unit cell calculated from the refinement of the PXRD,  $N_A$  is Avogadro's number and  $M$  is the molar mass of each element. The calculations have been done on constrained conditions that the transition metal oxide-doping is not compensated with oxygen vacancies. While the apparent density was measured using Archimedes method:

$$\rho_{\text{app}} = D/(M - S) \quad (3)$$

where  $D$  is the dry weight of the freshly fractured surface which is free from sharp edges, corners and cracks,  $S$  is the suspended mass after impregnation in boiled water for 5 h and  $M$  is the saturated mass of the tested specimen after removing all the excess water from the surface. PXRD measurements were done using a high temperature reactor chamber (Anton Paar XRD 900) with a count rate of 3 s per step at 0.05°. Mettler-Toledo equipment was used for thermogravimetric analysis in air as well as in 10%  $\text{H}_2$  balanced in  $\text{N}_2$  from room temperature till 1000 °C using a ramping rate of 5 °C min<sup>-1</sup> for both heating and cooling cycle. Scanning electron microscopy (SEM) coupled with energy dispersive X-ray (EDX; Philips XL 30) used for microstructure and composition analysis. Samples were sputter coated with Au thin film for SEM study.

### 2.3. Electrical conductivity studies

Electrical conductivity measurements were performed on sintered pellets in air,  $\text{N}_2$ , pure  $\text{H}_2$  and 30 ppm  $\text{H}_2\text{S}$  balanced in  $\text{H}_2$  using Pt and Au electrodes (Heraeus Inc., LP A88-11S, Germany). The grain interior and the grain-boundary conductivities were determined by using AC impedance spectroscopy (Solartron Electrochemical Impedance Spectroscopy; SI 1260, 100 mV; 0.01 Hz–1 MHz) in the temperature range from 300 to 800 °C. A two probe electrochemical quartz cell was used for measurements and data were collected during the heating and cooling cycles. The equivalent circuit elements analysis was done by ZView 3.3d software.

### 2.4. Surface structure analyses

Fourier transformed infrared spectroscopy (FTIR) was used for solid powdered samples by Varian instrument, Model FTS 7000 FTIR, equipped with DTGS detector. The data were collected in the transmittance mode within the spectral range from 4000 to 500 cm<sup>-1</sup> with 64 scan data accumulation and a resolution of 4 cm<sup>-1</sup>. A blank test was first carried out on a powder sample of dry pure KBr placed on an aluminum holder after degassing in vacuum at room temperature for 25 min. This preliminary treatment under vacuum is important before performing the test in order to get rid of the atmospheric  $\text{CO}_2$  species that adsorb on the surface of the sample and manifests a band at around 2350 cm<sup>-1</sup>. An adequate amount of the as-prepared and  $\text{H}_2\text{S}$ -treated samples were characterized after dispersing in KBr. Ultraviolet–visible (UV–vis) diffuse reflectance spectra (DRS) were performed using a Cary 5000 UV–

vis spectrophotometer (Varian) in the range of 200–800 nm where  $\text{BaSO}_4$  was used as a reference.

### 3. Results and discussion

#### 3.1. Structure characterization

**Fig. 1a** shows the PXRD patterns of as-prepared  $\text{Ce}_{0.9-x}\text{Y}_{0.1}\text{Mn}_x\text{O}_{2-\delta}$  ( $0 \leq x \leq 0.15$ ) (CYMO) by solid-state synthesis route at 1400 °C in air. All the prepared samples have the fluorite-lattice structure, with a space group  $Fm-3m$ . However, small peaks of a second phase  $\text{Mn}_3\text{O}_4$  (Joint Committee on Powder Diffraction Standards (JCPDS) # 01-072-7943) (**Fig. 1a**) were observed [15]. Impurity  $\text{Mn}_3\text{O}_4$  was also detected in the samples prepared via wet chemistry route over the entire range of doping, but to less extent than solid state method. **Fig. 1b** shows the PXRD pattern of the  $\text{Ce}_{0.8}\text{Y}_{0.1}\text{Mn}_{0.1}\text{O}_{2-\delta}$  prepared via co-precipitation and thermally treated at different temperatures. It is observed that the solid solution successfully formed at low temperature, i.e., 350 °C and shows fluorite-type structure. The shift in the peak position with increasing calcination temperature indicates the enhancement of solubility of Mn in the  $\text{CeO}_2$  lattice.

Introduction of Mn into CYO caused a slight shift in the diffraction pattern to higher  $2\theta$  angles that inferred a change in the lattice parameter due to a certain solubility of Mn in CYO. Kim et al. have proposed an empirical equation which describes the interrelationship between the lattice parameter of the fluorite-type structure and various parameters such as the concentration of defects, and ionic radius of dopants, as illustrated [20]:

$$a = 0.5413 + \sum_k m_k (0.022 \Delta r_k + 0.00015 \Delta z_k) \quad (5)$$

where,  $a$  (in nm) is the lattice constant of the ceria solid solution,  $\Delta r_k$  (in nm) is the difference in ionic radius ( $r_k - r_{\text{Ce}^{4+}}$ ) of the  $k$ th dopant and the  $\text{Ce}^{4+}$  radius, which in eight-fold coordination is 0.97 Å,  $\Delta z_k$  is the valence difference, ( $z_k - 4$ ), and  $m_k$  is the mole

percent of the  $k$ th dopant in the form of  $\text{MO}_x$ . The matching ionic radius is found to be 0.1106 nm for divalent cations and 0.1038 nm for trivalent ions. Upon substitution, Mn is expected to be in 2+ and/or 3+ oxidation states where ( $r_{\text{Mn}}^{2+}$  (VIII) = 0.96 nm and  $r_{\text{Mn}}^{3+}$  (VI) = 0.58 nm) [21] and Y has ionic radius ( $r_{\text{Y}}^{3+}$  (VIII) = 0.1019 nm) which is smaller than the critical ionic radius ( $r_c = 0.1038$  nm), thus, the addition of both Y and Mn tends to decrease the lattice constants. The solubility limit is controlled by the elastic energy in the strained structure in such a way that the minimum the strain the maximum the solubility of these elements and formation of solid solutions. The calculated lattice parameters presented in **Table 1** [22–27] for the parent and doped ceria samples prepared via wet chemistry route. A certain degree of doping as it is observed in case of 5–10 mol% Mn doping tends to decrease the lattice constants. We noticed that Mn insertion beyond 10 mol% has negligible effect on the lattice parameters. The calculated lattice parameter for CYO was closer to the values published in literature [28]. A slight variation in cell constant could be related to the different compositional distribution in the final product which is due to difference in preparation condition [29].

In the case of doping in  $\text{CeO}_2$ , the degree of solubility of different cations is presumably, dependent on the radius difference between the doped element and  $\text{Ce}^{4+}$  ions and the valence difference between them [30–32]. The low solubility of  $\text{Mn}_2\text{O}_3$  could be interpreted by the tendency to keep its orthorhombic structure of distorted octahedron oxygen lattice than eight-fold coordination site in the fluorite-type structure. Recently, it was suggested that the electronic structure of the TM is crucial to cause distortion in the fluorite lattice [33]. These structural parameters may add to the effect of small ionic radius to increase the configuration energy of the solid solution, and hamper further solubility of TM in ceria matrix. Thus, a small amount of TM may dissolved inside the ceria lattice and the remaining continue its segregation in the grain-boundary, as it is confirmed in some reported data for TM and rare earth-codoped ceria [34,35].

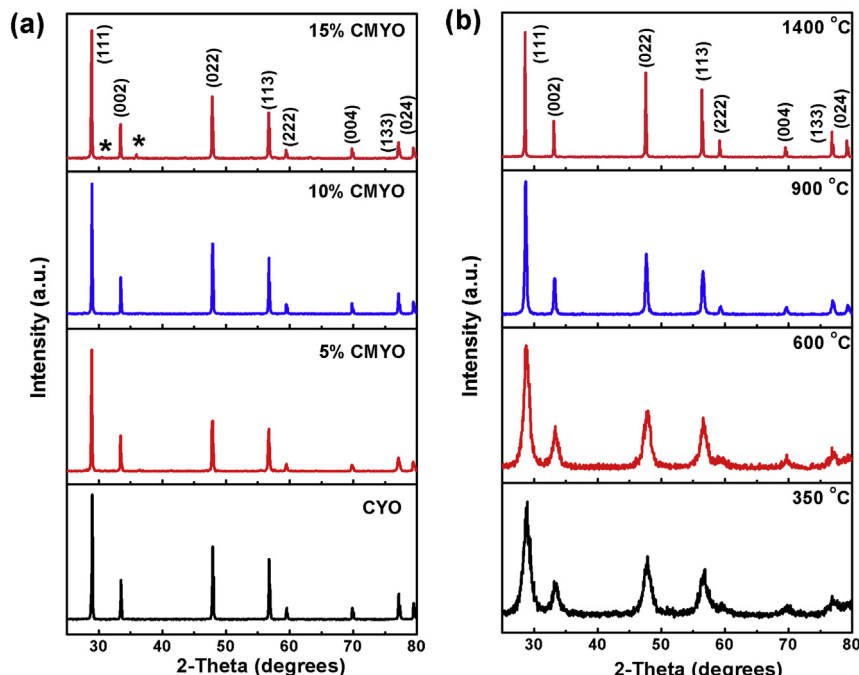


**Fig. 1.** PXRD of (a) the as-prepared  $\text{Ce}_{0.9}\text{Y}_{0.1}\text{O}_{2-\delta}$  (CYO) and Mn-doped  $\text{Ce}_{0.9-x}\text{Y}_{0.1}\text{Mn}_x\text{O}_{2-\delta}$  (CYMO,  $x = 5\text{--}15$  mol%) synthesized via conventional mixed solid state synthesis route and thermally treated at 1400 °C, and (b) 10% CYMO prepared with wet chemistry and calcined at different temperatures.

**Table 1**

The effect of different types of dopants on the electrical conductivity of cerium oxide in air.

Composition	Lattice parameter (Å)	Sintering temp. (°C)	$\sigma_{(600\text{ }^\circ\text{C})}$ (S cm <sup>-1</sup> )	$\sigma_{(700\text{ }^\circ\text{C})}$ (S cm <sup>-1</sup> )	$E_a$ (eV)
$\text{Ce}_{0.9}\text{Y}_{0.1}\text{O}_{2-\delta}$	5.408(1) [present]	1400	0.0052	0.0151	0.78
$\text{Ce}_{0.8}\text{Y}_{0.1}\text{Mn}_{0.1}\text{O}_{2-\delta}$	5.394(3) [present]	1400	0.0108	0.0619	1.07
$\text{Ce}_{0.9}\text{Mn}_{0.1}\text{O}_{2-\delta}$	5.400(2) [present]	1400	$1.5 \times 10^{-5}$	$4.0 \times 10^{-5}$	—
$\text{Ce}_{0.8}\text{Gd}_{0.2}\text{O}_{2-\delta}$	5.4229 [22]	1300	0.0235	0.0564	—
$\text{Ce}_{0.8}\text{Gd}_{0.12}\text{Nd}_{0.08}\text{O}_{2-\delta}$	5.4322 [22]	1300	0.0247	0.0626	—
$\text{Ce}_{0.8}\text{Gd}_{0.17}\text{Pr}_{0.03}\text{O}_{2-\delta}$	— [23]	1500	0.0094	0.0023	0.70
$\text{Ce}_{0.85}\text{Ca}_{0.05}\text{Sm}_{0.1}\text{O}_{2-\delta}$	5.3933 [24]	1450	0.0031	0.0054	0.64
$\text{Ce}_{0.8}\text{Sm}_{0.2}\text{O}_{2-\delta}$	5.4314 [25]	1300	0.0227	—	0.645
$\text{Ce}_{0.8}\text{Co}_{0.07}\text{Sm}_{0.13}\text{O}_{2-\delta}$	5.4259 [25]	1300	0.0538	—	0.567
$\text{Ce}_{0.8}\text{Gd}_{0.1}\text{Sm}_{0.1}\text{O}_{2-\delta}$	5.4302 [26]	1300–1400	0.0331	0.0065	0.59
$\text{Ce}_{0.8}\text{Gd}_{0.1}\text{Bi}_{0.1}\text{O}_{2-\delta}$	5.3940 [27]	1350	0.0270	0.0446	0.52

Electron spin resonance spectroscopy (ESR) and PXRD studies [36] displayed a weak possibility for the smaller size Mn<sup>3+</sup> to occupy 8-fold coordination site in the fluorite structure. XPS [37] spectra of the  $\text{Ce}_{0.9}\text{Mn}_{0.1}\text{O}_{1.95}$  prepared via wet combustion chemical route and thermally treated at 600 °C revealed distinctive peaks of binding energy corresponding to  $\text{Mn}_2\text{O}_3$ . Gupta et al. [37] inspected the emerged distortion in  $\text{CeO}_2$  upon doping with Mn cation through monitoring the distortion in the TM–O bond length and suggested that the solubility of TM is depending on how significant is the TM–O distortion in destabilizing the fluorite structure and the lattice strain. The beneficial effect of doping Mn in CYO has been emphasized through an enhancement in the relative density of doubly doped CYMO approaching 98% in comparison to CYO which is close to 65% at 1400 °C. The crystallite size was calculated to be within the range of 57–80 nm and addition of Mn has been proved to suppress the crystallite growth.

### 3.2. Microstructure

Fig. 2 shows that CYO prepared by co-precipitation (Fig. 2a) exhibits a homogenous morphology with a highly porous structure. The high porosity may be explained by the presence of some water molecules in the precipitate which resulted in agglomeration of the fine primary particles that possibly converted into hard agglomerates upon rising the temperature and were difficult to be sintered. Besides, the probability of presence of residual nitrates and ammonium species from precipitation that evaporate gases during their decomposition and may create more pores [38]. Even though the sample prepared by solid state reaction showed a higher density than soft chemistry route, it yields non-uniform particle size distributions and inter-granular porosity. These results were consolidated with the data published elsewhere [39,40]. The higher density of samples fabricated by solid–solid reaction is likely due to less agglomeration of the large particles of the starting materials.

CYMO samples prepared by both preparation methods have shown a radical change in the density as well as the morphology compared to Mn-free samples, as shown in Fig. 2. Addition of Mn helps improvement of the density with a pronounced effect on the samples prepared by wet chemistry route, as shown in the left panel of Fig. 2. The addition of  $\text{MnO}_2$  which is known to exhibit a lower melting point ~535 °C compared to ceria ~2400 °C, improves the densification by promotion of the atomic diffusion throughout the particle surface. The mechanism of sintering of ceramic powder is suggested to occur through liquid phase sintering. It was reported that the existence of an amorphous film of  $\text{CoO}$  that is sitting within the grain-boundary of Co-doped ceria is responsible for the rise in the observed density [41]. We believe that Mn has a similar effect on the sintering behavior as described above in case of Co despite the PXRD that did not show any peaks for the impurity phase at 5 mol% Mn doping in CYO (Fig. 1).

EDX shows that some grains are observed to exhibit spherical shape that have high content of Y reaches 30 mol% relative to Ce with negligible percent of Mn (Fig. 2c). In addition, two other shapes were detected in SEM images with rod-like and platelet that contain a high percent of Mn exceeds 40 mol% compared to Y and very small amount of Ce (Fig. 2c, g). The different morphologies observed in SEM images may be interpreted by the precipitation of  $\text{MnO}_x$  and  $\text{Y}_2\text{O}_3$  after reaching certain solubility in  $\text{CeO}_2$ . These macroscopic results suggest that Mn has low solubility in  $\text{CeO}_2$  Lattice, especially, when it is co-doped with rare-earth oxide [42–44]. This observation is in agreement with the PXRD which showed a secondary phase for all the doped samples irrespective to Mn content. Fig. 3 is presenting the SEM profile for  $\text{Ce}_{0.9}\text{Mn}_{0.1}\text{O}_{2-\delta}$  (CMO) where it shows highly dense structure and exhibiting a density of about 98%, as calculated from XRD. In addition EDX results confirmed homogeneous distribution of the elements without any sign for impurity phase.

### 3.3. Electronic structure

A diffuse reflectance spectrum (DRS) provides oxidation state and surface coordination of metal oxides by measuring  $d-d$ ,  $f-d$  transitions and also oxygen-metal ion charge transfer bands. Fig. 4 shows the diffuse reflectance spectra for the samples prepared by co-precipitation and calcined at 900 °C. Spectrum 1 of CYO (Fig. 4), manifests a characteristic absorption band analogous to that of pure  $\text{CeO}_2$  started around 370 nm which is due to charge transfer transition between  $\text{O}2p$  and  $\text{Ce}4f$  [45] which is abruptly decreased in intensity upon doping with 5 mol% Mn (Fig. 4(2)). A very weak absorption band in the UV region occurred with increasing Mn content (Fig. 4 (3 & 4)). Nevertheless, all the samples show a weak absorbance in the visible region. The spectra of the same compositions for the samples prepared with wet chemistry and calcined at 600 °C and solid ceramic method samples sintered at 1400 °C show the same absorption edge, which is not presented here. This indicates that co-precipitation is successful in synthesizing Mn, Y-doped  $\text{CeO}_2$  solid solutions at lower temperature.

The band structure of pure  $\text{CeO}_2$  is composed of valence band (VB) of oxygen 2p orbitals and a conduction band (CB) of cerium 5d whereas the 4f(Ce) orbitals are constituting an empty band that lies in between VB and CB with an optical band gap of 2.95 eV [46]. Doping  $\text{CeO}_2$  with Y resulted in insertion of 4d(Y) band which has a higher energy and is not involving in conduction. Rare-earth doping is known to introduce oxide ion vacancies in the anionic sub-lattice which has a slight effect on the position and width of the VB [47,48]. Mn addition may lead to introduce an impurity level above the VB which could faster the charge transfer, as in case of Pr-doped  $\text{CeO}_2$  [49].

The weakening in absorption band upon Mn-doping may be explained by two different assumptions. The decrease in absorption

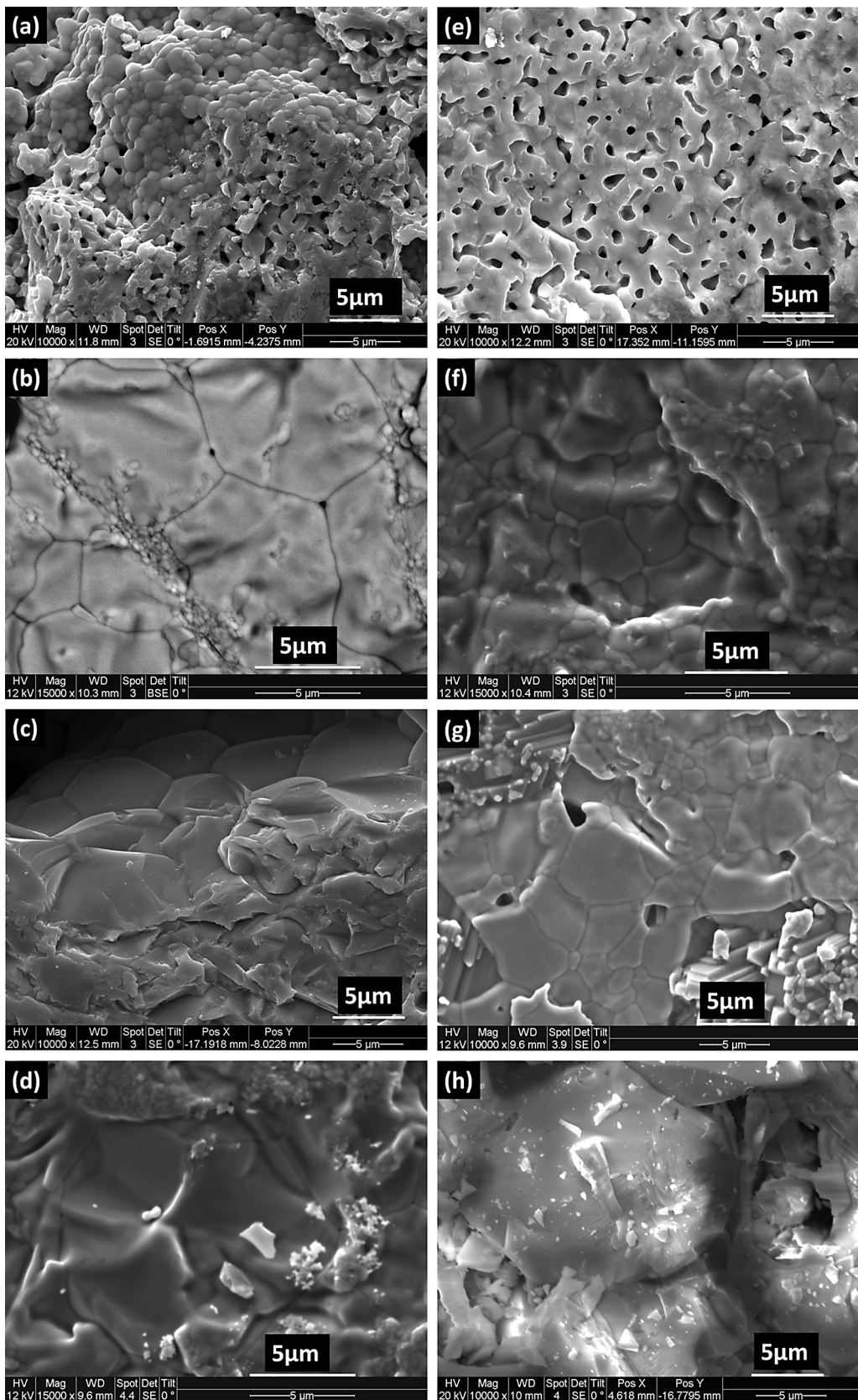


**Fig. 2.** Typical SEM images of polished, thermally etched surfaces of iso-statically pressed pellets and having a nominal composition of (a, e)  $\text{Ce}_{0.9}\text{Y}_{0.1}\text{O}_{2-\delta}$ , (b,f)  $\text{Ce}_{0.85}\text{Y}_{0.1}\text{Mn}_{0.5}\text{O}_{2-\delta}$ , (c, g)  $\text{Ce}_{0.8}\text{Y}_{0.1}\text{Mn}_{0.1}\text{O}_{2-\delta}$  and (d, h)  $\text{Ce}_{0.75}\text{Y}_{0.1}\text{Mn}_{0.15}\text{O}_{2-\delta}$  prepared by wet chemistry method (left panel) and solid state ceramic method (right panel) at 1400 °C.

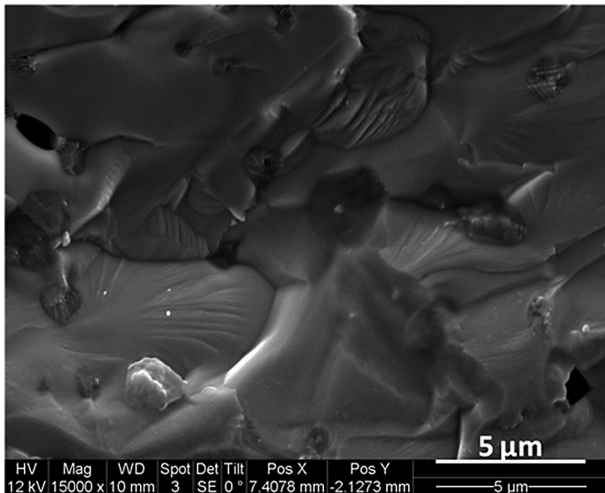


**Fig. 3.** Typical SEM images of polished, thermally etched surface of iso-statically pressed pellet of  $\text{Ce}_{0.9}\text{Mn}_{0.1}\text{O}_2$ .

edge in the CYMO samples may be discussed in terms of a certain role of Mn on altering the electronic structure of parent oxide i.e. CYO, which is a further reflectance of solubility of Mn in the fluorite lattice to form the solid solution. Corma et al. [50] has emphasized on the influential role of the oxide ion vacancy concentration on altering the width of the band gap. Furthermore, Guo group [51] has found that Sm and Gd-doped  $\text{CeO}_2$  gave rise to the intensity of absorption in the diffuse reflectance spectra compared to pure  $\text{CeO}_2$  in the UV region. However, they observed a decrease in the absorption band edge in the ceria samples doped with Pr or Tb. They claimed that fixed valent  $\text{Sm}^{3+}$  and  $\text{Gd}^{3+}$  cations have a tendency to crystallize in the dioxide or sesquioxide phases, which is similar to ceria structure, but without varying the band gap. In spite of that, mixed valence Tb or Pr phases exhibit different phases such as  $\text{Pr}_6\text{O}_{11}$  or  $\text{Tb}_4\text{O}_7$  which may affect the band gap. The obtained optical spectra could be due to electronic transitions either between crystal field states, or the valence to conduction band and also through ligand to metal charge transfer. Thus, mixed valence oxidation state cations can give rise to donor and acceptor levels in the forbidden energy band, tends to shift the absorption edge and/

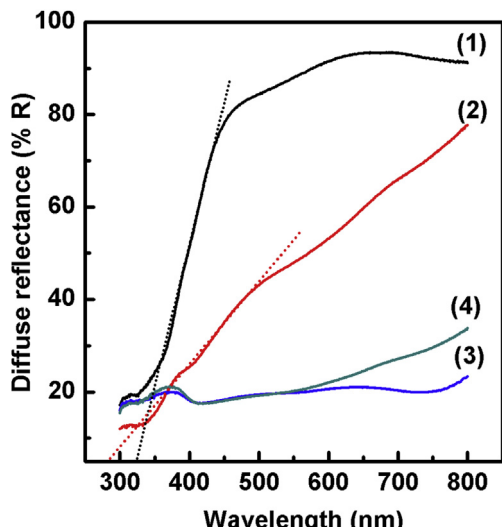


**Fig. 4.** UV-vis diffuse reflectance spectra measured in ambient air of 1) CYO, 2) 5% CYMO, 3) 10% CYMO, and 4) 15% CYMO samples prepared by coprecipitation and calcined at  $900^\circ\text{C}$  in atmospheric pressure.

or interaction of the electron density of the host lattice with the dopant may cause a lowering in the electron energies with additional downward shift in the conduction band to generate a distorted band structure. These results trigger us to assume that substitution of  $\text{Ce}^{4+}$  with Mn could lead to a decrease in the oxygen vacancies, and enhancement of electronic transport properties.

Another scenario is suggesting that the surface of CYMO may be covered with  $\text{MnO}_x$ , which does not show any reflectance maxima due to absence of crystal field splitting. Beside, the appearance of the spectrum of 10 and 15 mol% Mn doped CYO which is resembles in its shape to the spectrum recorded for pure  $\text{MnO}_2$ . The increase in absorbance of 5 mol% Mn in comparison to 10 CYMO and 15 CYMO in the visible region may indicate the presence of Mn in another oxidation state [52]. We attempted to calculate the optical band gap ( $E_g$ ) for our samples by determining the cut-off wavelength. This was done by extrapolating the linear part of the steep rise line in the curve- that occurs at energies closer to the band gap of the material- to intersect with the wavelength represented by the x-axis, and using the energy of the incident photon.  $E_g$  was found to be 3.54 eV and 3.87 eV for CYO and 5 mol% CYMO, respectively. The higher value of  $E_g$  for Mn-doped sample may indicate the insulating behavior of the impurity phase of  $\text{MnO}_x$ .

### 3.4. Electrical conductivity

The electrical conductivity ( $\sigma$ ) depends on the concentration ( $n$ ), and electrical mobility ( $\mu$ ) of the charge carrier species and elementary charge ( $q$ ) as:

$$\sigma = nq\mu \quad (6)$$

Pure  $\text{CeO}_2$  is a poor ionic conductor, while doping with acceptor dopants such as alkaline earth or rare earth oxide was acknowledged to have frequently a better solubility and also improves its electrical conductivity significantly. Addition of lower valence cations was found to create mobile oxide ion vacancies in the fluorite lattice and the degree of ionicity was explained by the difference in the strength of trapping vacancies by the dopant cation [53]. This could rationalize the strong dependence of ionic conductivity on the dopant type and concentration that causes the distortions in the lattice. Kilner and Brook [54] correlated the highest conductivity in the oxides of fluorite structure to the dopant that results in the minimum stress in the host lattice. Another parameter could be the distortion in the local structure of the oxygen sub-lattice and cation-oxygen bond length. Accordingly, local structure of both the host and the guest cations influence the ability of the resultant solid solution to undergo reduction as well as the ordering of oxygen which determine the electrical conductivity.

Fig. 5 shows typical AC impedance plots of the investigated doped  $\text{CeO}_2$  in air and  $\text{H}_2$  at  $510^\circ\text{C}$ . The low-frequency intercept ( $R$ ) to the real axis was used to determine the total electrical conductivity using the relationship:

$$\sigma = \left( \frac{1}{R} \right) \left[ \frac{L}{A} \right] \quad (7)$$

where  $L$  and  $A$  represent thickness and area of the investigated ceria samples, respectively. The absence of low-frequency tail in case of CMO indicates non-blocking nature of the electrode-ceramic interface. The bulk and the grain-boundary for Mn-doped  $\text{CeO}_2$  were found to have higher total resistivity compared to CYO at intermediate temperature in air (Fig. 5a). However, electrical conductivity for both samples approaching each other as seen in (Fig. 5c) at  $510^\circ\text{C}$  in  $\text{H}_2$ . At  $700^\circ\text{C}$ , in  $\text{H}_2$ , The conductivity of CMO

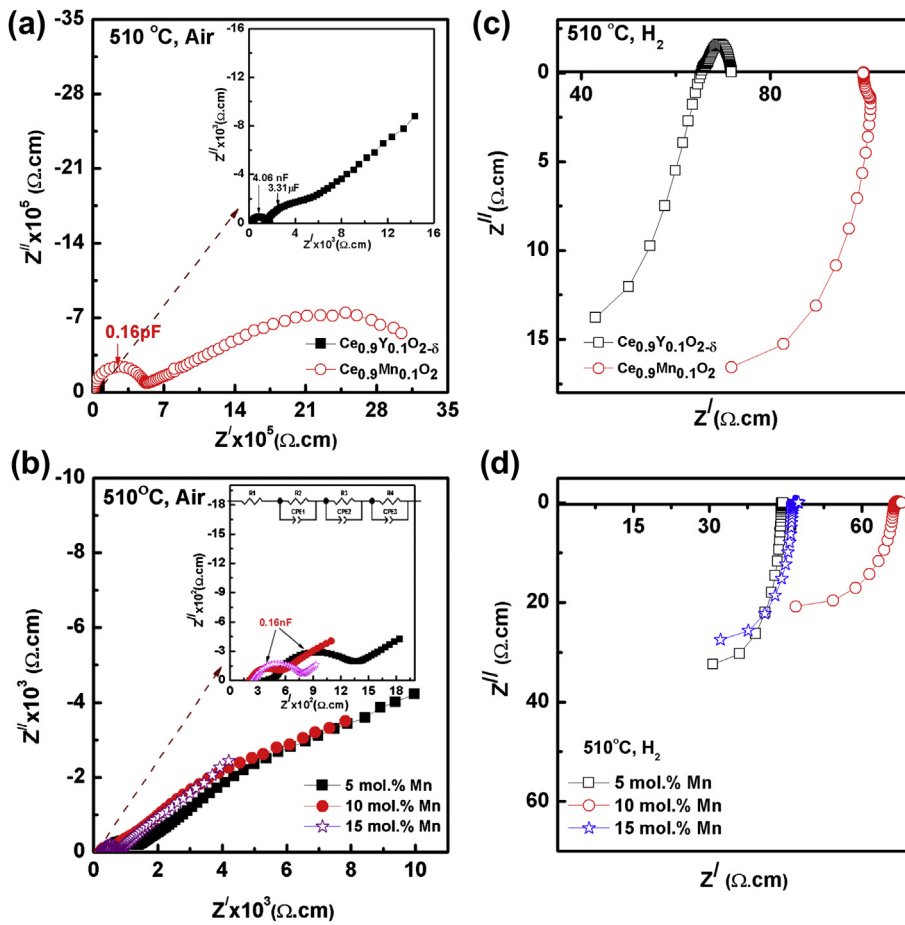


**Fig. 5.** Normalized AC impedance spectra of (a,c) Ce<sub>0.9</sub>Y<sub>0.1</sub>O<sub>2-δ</sub> (CYO) and Ce<sub>0.9</sub>Mn<sub>0.1</sub>O<sub>2-δ</sub> and (b,d) Ce<sub>0.8-x</sub>Y<sub>0.1</sub>Mn<sub>x</sub>O<sub>2-δ</sub> ( $x = 5\text{--}15\text{ mol\% Mn}$ ) (CYMO) prepared via coprecipitation and measured in air and pure dry H<sub>2</sub>. The inset graph represent the magnified impedance plot for (a) CYO and (b) CYMO at higher frequencies, and the equivalent circuit used to fit the data (Fig. 5b).

exceeds that of CYO with one order of magnitude. This is expected due to the reduction of more Mn together with Ce, consequently; adding the electronic contribution to the total conductivity. The total conductivity for CMO is estimated to be  $4 \times 10^{-5} \text{ S cm}^{-1}$  and  $0.13 \text{ S cm}^{-1}$  at 700 °C in air and H<sub>2</sub>, respectively. Likewise, CYO conductivity was calculated to be  $0.01 \text{ S cm}^{-1}$  and  $0.012 \text{ S cm}^{-1}$  at 700 °C in air and H<sub>2</sub>, respectively.

In order to quantify the effect of Mn addition on the total electrical impedance, fitting of the measured AC impedance spectra was performed based on Brick layer model, using an equivalent circuit, as shown in Fig. 5. R-CPE (constant phase element) was used to describe the depressed semicircle. CPE represents non-ideal capacitor. At low temperature, well-resolved bulk and grain-boundary arcs are obtained at higher and intermediate frequencies with a spike at lower frequency attributed to electrode polarization. However, at higher temperatures such as 510 °C (Fig. 5b), only one arc is considered.

Fig. 5b and d displays the influence of introduction of Mn on the impedance at 510 °C in air and H<sub>2</sub>. For 5–15 mol% Mn doping, Fig. 5b has shown that Mn has no effect on the grain conductivity, while a great enhancement on the grain-boundary conduction is clear in air, which suggests that the grain-boundary impedance may be controlled by TM [55]. Adding sintering aid such as MnO<sub>x</sub> improves the densification of ceria based samples and facilitates the oxide ion migration. The presence of segregation of Mn-rich phase in the grain-boundary may act as electronic paths and promote the electronic conductivity. We speculate that these MnO<sub>x</sub>

phases are disconnected so that it will not impede the path of the oxide ion which is verified from the lower resistivity values of grain-boundaries of Mn doped compared to Mn-free CYO. As seen in Fig. 5d, all the Mn-doped samples show a lower resistivity in reducing atmosphere compared to air.

Fig. 6 demonstrates the Arrhenius plots of the total electrical conductivity of CYMO prepared through solid state method (left panel) and wet chemistry method (right panel), and measured in air and H<sub>2</sub>, respectively. The electrical conductivity value is the highest in the sample doped with 10 mol% Mn, reaching  $0.03 \text{ S cm}^{-1}$  and  $0.06 \text{ S cm}^{-1}$  at 700 °C in air for powders prepared via wet chemistry and solid state chemistry route, respectively. While in H<sub>2</sub>, the electrical conductivity is almost the same ca,  $0.15 \text{ S cm}^{-1}$  at 700 °C irrelevant to the method of preparation, which has been previously reported [53]. In view of this data, the conductivity of the samples prepared via solid state chemistry shows higher numerical values relative to the ones prepared via coprecipitation. However, higher average activation energy of 1.07 eV is observed for the 10-CYMO sample prepared in air by solid state reaction versus 0.62 eV for its analogous that is prepared via soft chemistry route.

The electrical conductivity ( $\sigma$ ) can be related to both activation energy ( $E_a$ ) and pre-exponential factor ( $\sigma_0$ ) which are dependent on the concentration of charge carriers [56]:

$$\sigma T = \sigma_0 \exp \left( \frac{-E_a}{k_B T} \right) \quad (8)$$

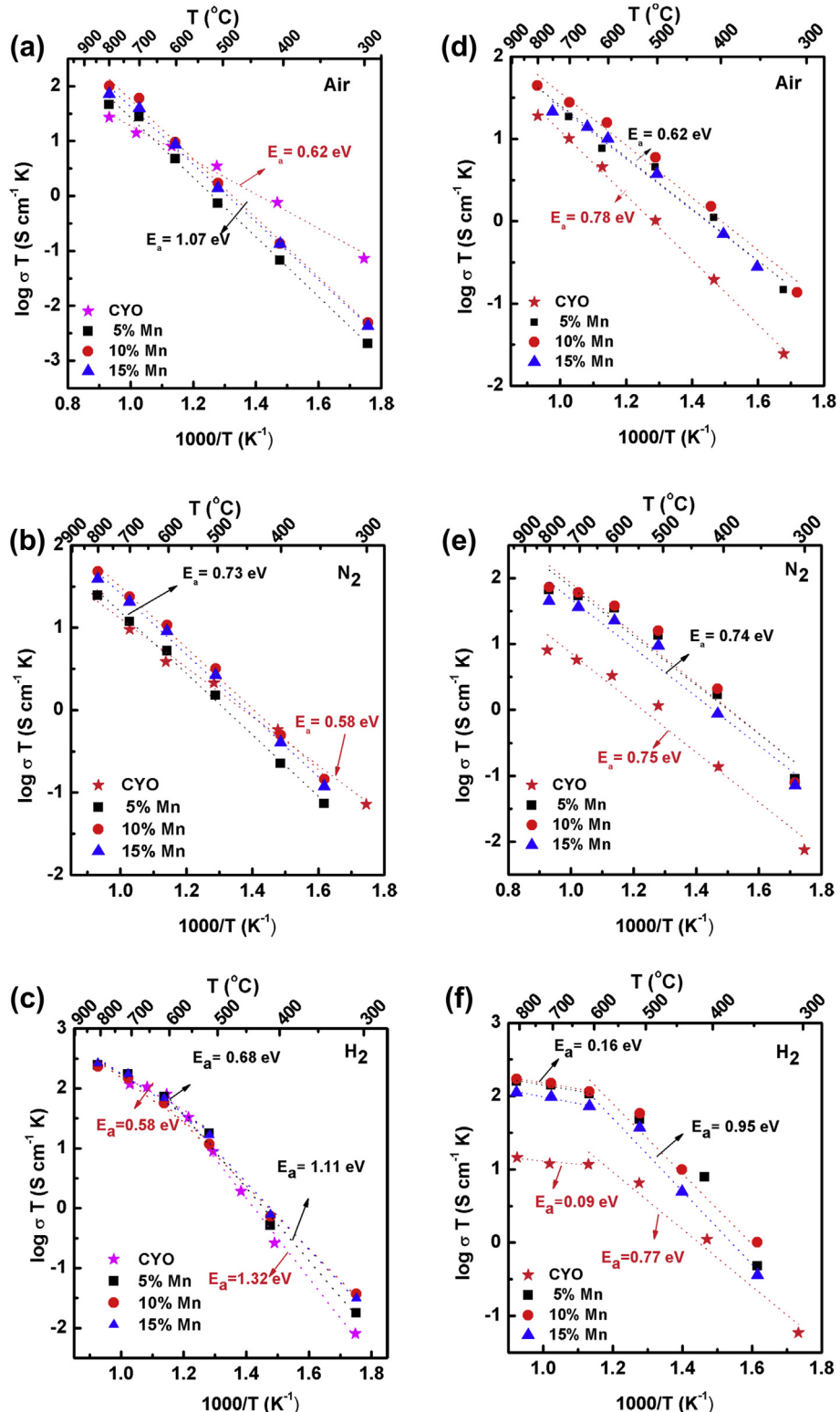


**Fig. 6.** The total conductivity as a function of temperature presented as Arrhenius plot for  $\text{Ce}_{0.9-x}\text{Y}_{0.1}\text{Mn}_x\text{O}_{2-\delta}$  sintered pellets with different Mn loading ( $x = 0\text{--}15$  mol%) and Pt electrodes under different atmospheres. (a–c) Samples prepared via conventional mixed solid state route, and (d–f) samples prepared wet chemistry route. Broken lines passing through the data points represent best fit.

where  $T$  is the absolute temperature and  $k_B$  is the Boltzmann constant. Thus, it could be concluded that the difference in conductivity values of the same composition prepared by two different methods could be discussed in terms of the change in the micro-structure of the prepared samples, i.e. the particle size, porosity and

the compositional distribution of the dopant. All the aforementioned parameters will have a serious impact on the mobility of both ionic and electronic species.

At temperature range from 300 to 600 °C the activation energy for solid state CYMO is 1.11 eV versus 0.95 eV for wet chemistry in

$H_2$ , while in temperature range 600–800 °C it shows average value of 0.7 eV versus 0.16 eV in  $H_2$ . The origin of the two slopes could be interpreted based on the fact that the ionic conductivity of rare earth-doped  $CeO_2$  is an impurity controlled conduction mechanism and  $pO_2$  independent [57]. The activation energy of oxygen diffusion at lower temperature will be a combination of the thermal energy required to dissociate the defect cluster formed between anion vacancies and cations due to electrostatic interaction in addition to the migration energy of the free anion vacancies. It may be confessed that at high temperature only the enthalpy of migration is valid [54,58]. We also anticipate that the decrease in activation energy at higher temperature in  $H_2$  might be due to the lowering in the enthalpy of migration of ions and electrons (i.e., fast mobility) and reduction in the enthalpy of formation of redox species (i.e.  $Mn^{3+}/Mn^{2+}$  and  $Ce^{4+}/Ce^{3+}$ ) which tend to increase the concentration of the electrons.

The higher values in activation energy at lower temperature range in  $H_2$  relative to air could be a result of the lower  $pO_2$  that may result in a loss of surface oxygen and a reduction of Mn with the chance of creating more oxygen vacancies. It has shown in literature [58–61] that  $CeO_2$  grain-boundary core is rich with oxygen vacancies which make it more positive compared to the space charge layer. They claimed that the substitution of  $Ce^{4+}$  with lower valent TM tends to introduce more negative charges which partially work to counterbalance the positive core charge and could alter the charge distribution in the space charge layer. This hypothesis is applicable if the concentration of TM is sufficiently low and a second phase is absent. In the present study, a second phase was detected in the samples, which is apparently affecting the conduction mechanism. Thereby, it is crucial to correlate the electrical behavior of doped  $CeO_2$  to the effective size and the local structure of the dopant at different temperatures with emphasizing on the effect of stressed structure on the segregation of dopant as a second phase to release the strain. A comparison graph for selected examples of doped  $CeO_2$  systems is presented in Fig. 7. As it is clear that this work shows higher conductivity values compared to the literature [38,43,62,63].

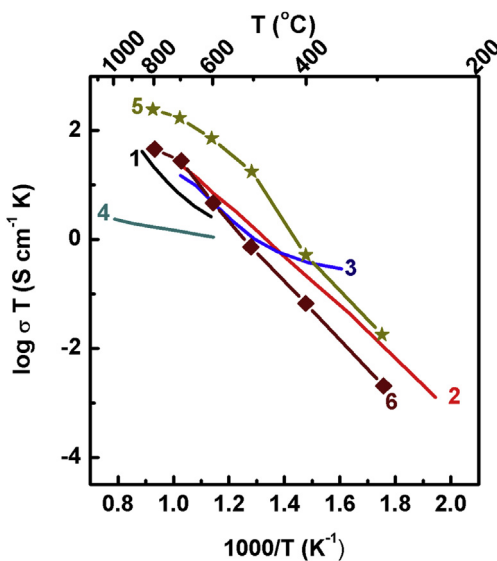


**Fig. 7.** A comparison graph represents the change in total conductivity as a function of temperature of the present work vs. some reported ceramic samples of composition: (1) 1 at.% Mn-doped  $Ce_{0.8-x}Gd_{0.2-x}O_{2-\delta}$ , [43] (2) 0.5 at.% Mn-doped  $Ce_{0.8-x}Gd_{0.2-x}O_{2-\delta}$ , [62] (3) 2 mol.%  $Ce_{0.9-x}Gd_{0.1}O_{2-\delta}$ , [63] (4) 15 mol.% Mn-doped  $CeO_{2-\delta}$ , [36] and ([5,6], present work)  $Ce_{0.85}Y_{0.1}O_{2-\delta}$ ; where all the samples measured in air except sample 6 which has been measured in pure  $H_2$ .

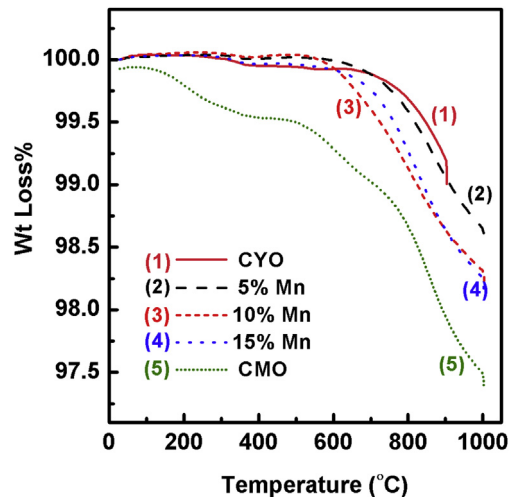


**Fig. 8.** TG curve for  $Ce_{0.9-x}Y_{0.1}Mn_xO_{2-\delta}$  (where:  $x = 0–15$  mol %) samples prepared with conventional mixed solid state synthesis route, sintered at 1400 °C and thermally treated with a ramping rate 5 °C min<sup>-1</sup> under 10%  $H_2$  balanced in  $N_2$ .

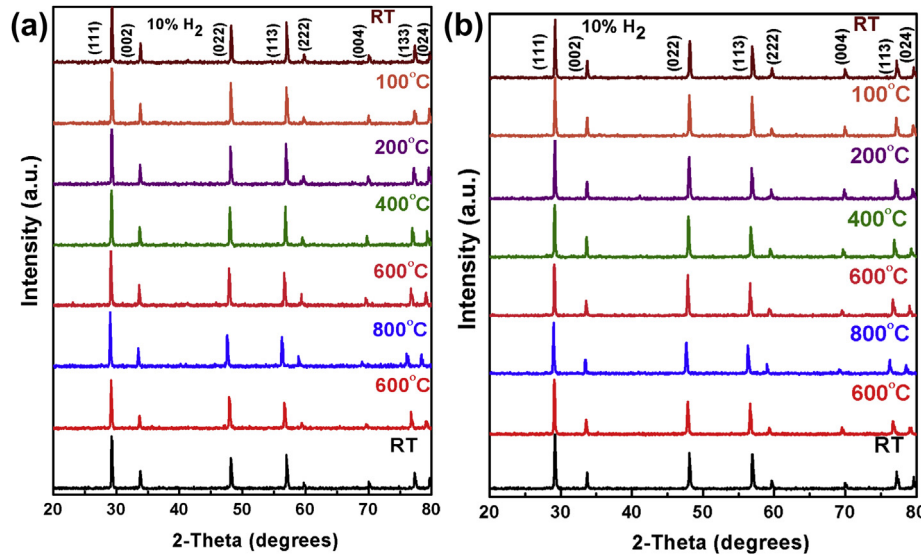
### 3.5. Thermal analyses

Fig. 8 represents the TGA of a series of doped  $CeO_2$  which was measured in 10%  $H_2$  balanced in  $N_2$ . Doping of  $CeO_2$  with Mn alone results in two stages weight loss. A weight loss starts around 100 °C and extends till 400 °C, and a second continuous loss above 500 °C. The first decrease in weight could be due to potential surface reduction of  $Ce^{4+}$  to  $Ce^{3+}$  in addition to Mn reduction, while the second one around 500 °C is interpreted to bulk reduction of  $CeO_2$ . However, TG curve of CYO manifests a decrease in weight commences close to 700 °C and extends till 1000 °C in dry  $H_2$ . Addition of Y tends to shift the reduction temperature of the  $Ce^{4+}/Ce^{3+}$  couples which usually occurs in pure ceria at 600 °C and is consistent with the reported results for different rare-earth-doped ceria [64].

In contrast, Mn incorporation together with Y in ceria lattice is responsible for substantial reducibility of the solid solution. It is noticeable that the reduction starts earlier in the sample that is containing high percent of Mn. A marginal change in the reduction temperature with almost zero change in the percent of weight loss occurs with lowering Mn content compared to CYO. Zajac and Molenda [64] assumed that a distortion in the oxide ion network affect the reducibility. They suggested that the presence of free oxide vacancies in the solid solution lattice resists the reduction, while cluster formation resulted from high rare-earth concentration doping facilitates the reduction and lower its temperature. Insertion of Mn cation into Y-doped  $CeO_2$  has a slight modification on the redox stability of the solid solution compared to free CYO, which implies that Mn percent in the lattice is low. Also the concurrent results shed the light on the fact that the mechanism of insertion of Mn into  $CeO_2$  is different than the situation in the presence of rare earth oxide. It is ambiguous to not see the earlier reduction step in samples containing both Mn and Y cations during exposure to hydrogen in the heating cycle. This may guide to an assumption that presence of Y and Mn together tends to form a stable compound that exhibit the cubic structure and stabilize the Mn in a fixed oxidation state. There is a consistency between our results for TM and RE cations doped  $CeO_2$  and the results from temperature program reduction done by Gupta et al. [37].

### 3.6. HT-PXRD and TEC evaluation

High temperature PXRD was employed to investigate the structure changes and stability of pure and doped CYO under



**Fig. 9.** High-temperature XRD pattern for (a)  $\text{Ce}_{0.8}\text{Y}_{0.1}\text{Mn}_{0.1}\text{O}_{2-\delta}$  and (b)  $\text{Ce}_{0.9}\text{Mn}_{0.1}\text{O}_{2-\delta}$  powders prepared via conventional mixed solid state synthesis route and measured in 10%  $\text{H}_2$  balanced in  $\text{N}_2$  and thermally treated with a ramping rate for heating and cooling  $6\text{ }^{\circ}\text{C min}^{-1}$ .

ambient air and 10%  $\text{H}_2$  mixed in  $\text{N}_2$  at 373–1073 K (Fig. 9). The average lattice thermal expansion ( $\alpha$ ) of the samples under investigations was calculated from the line of best fit of the graph ( $\Delta L/L_0$  vs. Temp. (Fig. 10)).

$$\alpha_{T-T_0} = \left( \frac{\Delta L}{L_0} \right) \left( \frac{1}{T-T_0} \right) \quad (9)$$

$\Delta L/L_0$  represents the ratio between the relative changes in the lattice parameter of  $\text{CeO}_2$  i.e.,  $(a - a_0)/a_0$ , at a specific temperature ( $T$ ) compared to its value at room temperature ( $T_0$ ). Here, we assumed zero lattice expansion at 298 K and the lattice constants recorded for powder samples will result in lattice expansion that is slightly different from the linear expansion coefficient measured using pellets due to presence of defects at the surfaces and interfaces that might affect the expansion process.

HT-XRD profile in Fig. 9 for CYMO and CMO shows that the fluorite structure is maintained over the temperature range of study under reducing condition. Absence of peaks related to any impurity or phase separation is confirmed. A shift in peak position is observed which might correlate with the thermal and chemical

expansion evolved upon rising the temperature and the value of shift shrinks with decreasing the temperature under 10%  $\text{H}_2$  in  $\text{N}_2$ . However, it is not fully reversible. The lattice expansion occurs at high temperature and under reducing conditions could be due to an increment of vacancies upon oxygen removal from the lattice and creation of  $\text{Ce}^{3+}$  which has a bigger size than  $\text{Ce}^{4+}$  and the change in Mn oxidation state. This type of expansion is called chemical expansion and is dependent on the oxygen non-stoichiometry ( $\delta$ ) and redox stability of the cations in the tested lattice [65]. The thermal expansion is described to be due to the electrostatic interactions between the different charged species in the lattice and is a function of their concentration and thermal lattice vibrations [66]. The TEC is, thus, the result of the combination between thermal and chemical expansion and the defect interactions between the dopant and host. It is worth to mention here that the anion vacancies in fluorite structure have a subtle effect on the value of TEC over a range of temperature and  $p\text{O}_2$ .

The advantage of operating HTXRD under reducing conditions enabled us to calculate the average TEC from the slope of the relationship between  $\Delta L/L_0$  as a function of temperature (Fig. 10). The data extracted from the graph was compared with the TEC the

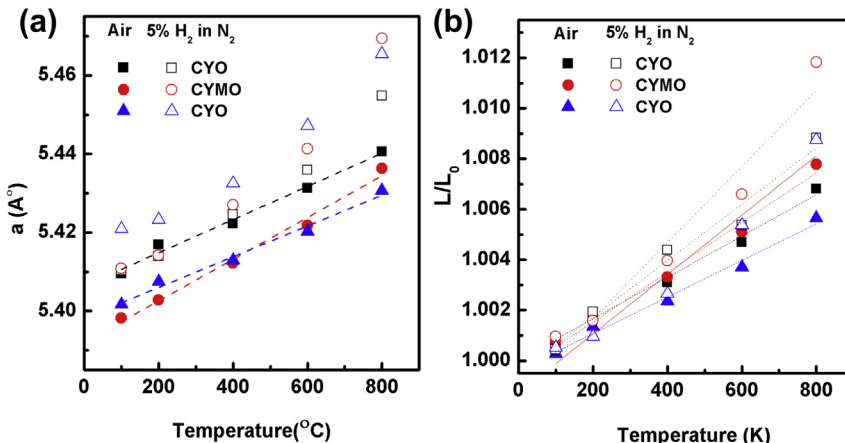


**Fig. 10.** Variation of (a) lattice constants and (b) lattice thermal expansion refined from the pattern recorded by HT-XRD as a function of temperature; where the closed symbols represent the data measured in air while the open symbols represent the data measured in 10%  $\text{H}_2$  in  $\text{N}_2$  for  $\text{Ce}_{0.9}\text{Y}_{0.1}\text{O}_{2-\delta}$  (square),  $\text{Ce}_{0.8}\text{Y}_{0.1}\text{Mn}_{0.1}\text{O}_{2-\delta}$  (circle) and  $\text{Ce}_{0.9}\text{Mn}_{0.1}\text{O}_{2-\delta}$  (triangle). Broken lines passing through the data points represent best fit.

literature values that measured in air (Table 2) [43,67–71]. The TEC of CYO was found to be the lowest among other rare earth-doped  $\text{CeO}_2$  since TEC increases with the increase in ionic radius and cation contents [67]. Also the variations in the measured lattice parameters of CYO in air as a function of temperature was in consistent with the data published elsewhere [28]. Addition of Mn in CYO results in contraction of the lattice volume and shows the same reported trend for Mn-doped GDC (Table 2). Moreover, it was found that CYMO samples acquired higher value for TEC than in CYO and CMO. In general, The TEC data measured through this work using HTXRD (Table 2) is closer to the literature values [43,67,69–71]. The differences may be attributed to the instrumental errors such as temperature gradient between the sample temperature and the thermocouple, and alignment of the high temperature stage. Chemical expansion correlated to vacancy concentration, and microstructural differences between the samples prepared by various synthetic routes and sintering temperatures could also be contributing factors for the observed conflict between the estimated TEC in the present work and literature values (Table 2).

### 3.7. Chemical stability in 30 ppm $\text{H}_2\text{S}$ in $\text{H}_2$

The electrical conductivity of all the samples measured under  $\text{H}_2\text{S}$  balanced in  $\text{H}_2$  shows relatively higher values after 600 °C compared to their values in pure  $\text{H}_2$ , as seen in (Fig. 11). Mn-doped  $\text{CeO}_2$  and 10% CYMO have shown more than 3 orders of magnitude higher conductivity after sulfur exposure at 300 °C than in  $\text{H}_2$ . This clarifies the significant role of Mn in improving the sulfur absorptivity. The closer values of conductivity measured in  $\text{H}_2$  versus ones that measured in  $\text{H}_2\text{S}/\text{H}_2$  at 600 °C may plausibly be due to the reversible adsorption–desorption of sulfur.

PXRD shows that CYMO and CMO samples retained fluorite structure after  $\text{H}_2\text{S}$  exposure. No impurity peak for a second phase, a separate manganese oxide or  $\text{Ce}_2\text{O}_2\text{S}$  was detected. GDC has also shown the same behavior as CYO. A shift in peak position occurs as seen in comparison with the sample measured in air (Fig. 12). This shift is explained by the fact that  $\text{Ce}^{4+}$  is converted into  $\text{Ce}^{3+}$  under this reducing environment. It is known that  $\text{H}_2\text{S}$  levels up to 450 ppm has no effect on the performance of  $\text{CeO}_2$ -based anodes [72,73]. Thus, it can be concluded that doping  $\text{CeO}_2$  with both rare-earth and manganese oxide did not affect the tolerance of  $\text{CeO}_2$  to  $\text{H}_2\text{S}$  poisoning. Fig. 13 shows the SEM images for surface and cross section areas of free and doped pellets after their treatment with

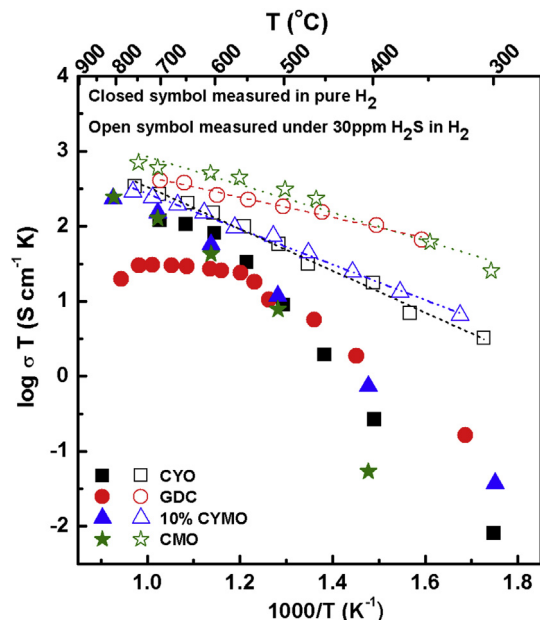


**Fig. 11.** Total electrical conductivity of different solid solutions of ceria based compounds measured in  $\text{H}_2$  as well as 30 ppm  $\text{H}_2\text{S}$  in  $\text{H}_2$ . Broken lines passing through the data points represent best fit.

sulfur contained atmosphere at high temperature. All the pellets including the commercial GDC manifest different range of sulfur distribution in the surface and bulk.

### 3.8. FT-IR measurements

Solid materials usually exhibit heterogeneous distribution of surface energy, where gases or liquid molecules tend to attach to the surface. Thus, FTIR is considered as an important tool to provide a thorough understanding of the surface structure as it permits direct monitoring of the interaction between adsorbate molecules and adsorbent solid surfaces. Here, we have investigated the surface properties of a series of doped-  $\text{CeO}_2$  samples before and after exposure to 30 ppm  $\text{H}_2\text{S}$  balanced in  $\text{H}_2$  using IR in the spectral range from 4000 to 500  $\text{cm}^{-1}$  at room temperature. Also, to tackle the problem of Mn that exhibits a variety of valences and prone to

**Table 2**

The estimated relative expansion coefficient from HT-XRD data compared to the reported ones.

Composition	$a$ (Å) at RT	$\alpha$ (K) $\times 10^{-6}$		Method	Temp. range (K)
		Air	10% $\text{H}_2 + \text{N}_2$		
$\text{Ce}_{0.9}\text{Y}_{0.1}\text{O}_{1.9}$	5.408(1)	8.2	11.2	HTXRD [present]	373–1073
$\text{Ce}_{0.8}\text{Y}_{0.1}\text{Mn}_{0.1}\text{O}_{1.9}$	5.394 (3)	9.9	15.1		
$\text{Ce}_{0.9}\text{Mn}_{0.1}\text{O}_{1.9}$	5.400 (2)	7.3	11.8		
$\text{CeO}_2$	5.4113	10.7	–	TMA <sup>a</sup> [67]	298–800
$\text{Ce}_{0.8}\text{La}_{0.2}\text{O}_{1.9}$	5.4776	11.7	–		
$\text{Ce}_{0.8}\text{Sm}_{0.2}\text{O}_{1.9}$	5.4370	11.1	–		
$\text{Ce}_{0.8}\text{Dy}_{0.2}\text{O}_{1.9}$	5.4112	10.9	–		
$\text{Ce}_{0.8}\text{Yb}_{0.2}\text{O}_{1.9}$	5.3897	10.8	–		
$\text{Ce}_{0.8}\text{Gd}_{0.2}\text{O}_{1.9}$	5.4225	12.0	–	Dilatometer [43]	298–1170
$(\text{Ce}_{0.8}\text{Gd}_{0.2}\text{O}_{1.9})_{0.99}(\text{Mn}_2\text{O}_3)_{0.01}$	5.4185	11.9	–		
$(\text{Ce}_{0.8}\text{Gd}_{0.2}\text{O}_{1.9})_{0.99}(\text{Co}_2\text{O}_3)_{0.01}$	5.4221	11.5	–		
$(\text{Ce}_{0.8}\text{Gd}_{0.2}\text{O}_{1.9})_{0.99}(\text{Fe}_2\text{O}_3)_{0.01}$	5.4229	12.3	–		
$(\text{Ce}_{0.8}\text{Gd}_{0.2}\text{O}_{1.9})_{0.99}(\text{TiO}_2)_{0.01}$	5.4232	12.3	–		
$\text{CeO}_2$	5.4111	12.68	–	HT-XRD [81]	293–1473
$\text{Y}_2\text{O}_3$	10.604	8	–	Dilatometer [70,71]	293–1123
$\text{Ce}_{0.85}\text{Y}_{0.15}\text{O}_{2-\delta}$	5.4066	11.02	–	Dilatometer [70]	293–1123

<sup>a</sup> TMA: thermomechanical analysis.

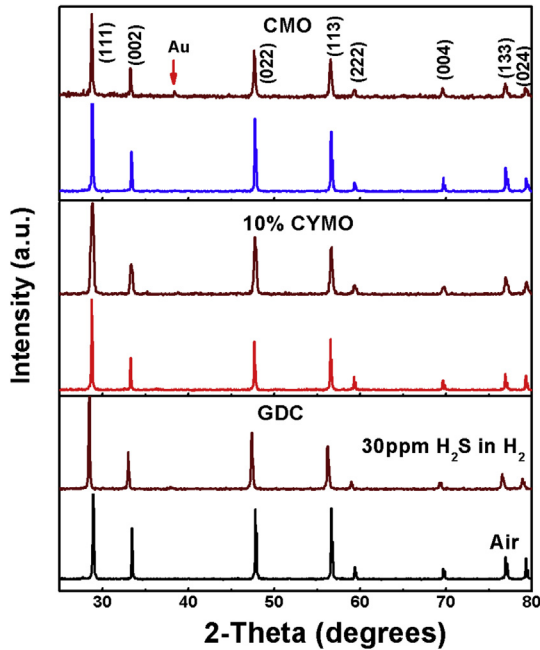


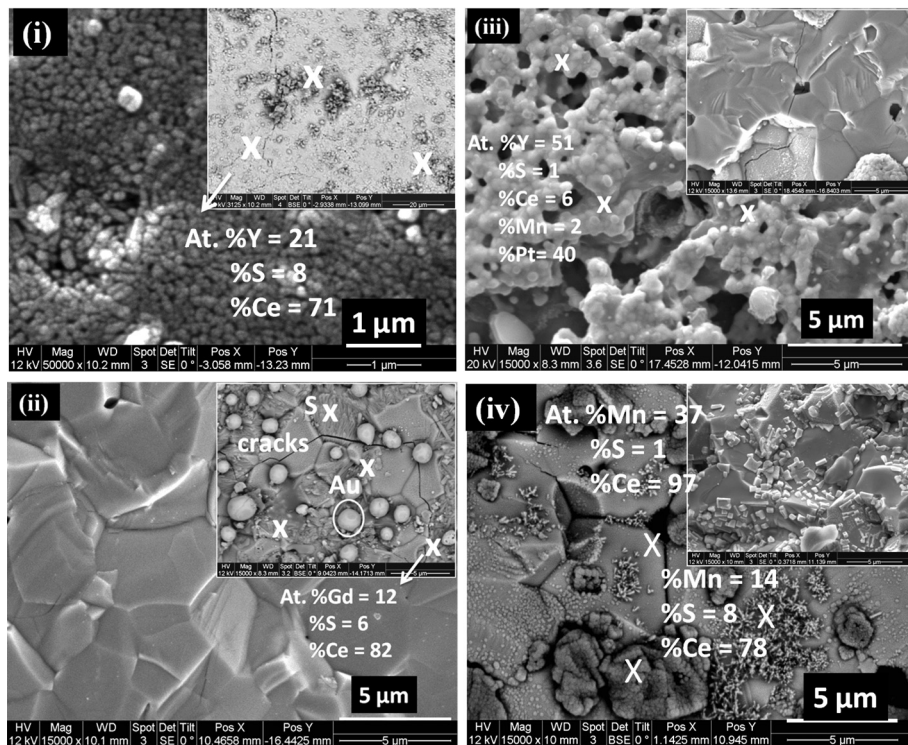
**Fig. 12.** Room temperature PXRD pattern of ceria samples after exposure to 30 ppm H<sub>2</sub>S balanced in H<sub>2</sub> at temperature range 300–800 °C for 48 h. PXRD pattern of the as-prepared samples is shown for comparison.

change it under specific conditions. In Fig. 14(I), it was clear that all the spectra exhibit the same number of bands localized approximately at the same position irrespective of the type of dopants. The prominent band centered at 3478 cm<sup>-1</sup> was assigned to the tridentate OH groups [74,75]. A weak small band at 2353 cm<sup>-1</sup> was

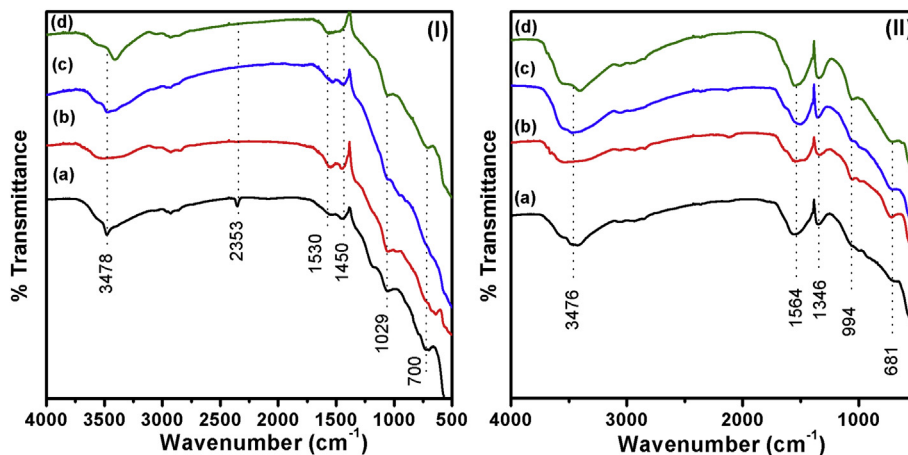
apparently due to residual atmospheric CO<sub>2</sub> still present after outgassing under vacuum for 30 min at room temperature. All bands at 1600 cm<sup>-1</sup> to 1000 cm<sup>-1</sup> may be either due to OH group or residual carbonate species which are assumed to be there due to the basic nature of CeO<sub>2</sub> which possesses weak Lewis acid site strength [76]. The bands at 1029 cm<sup>-1</sup> and that around 700 cm<sup>-1</sup> are postulated to be  $\delta(\text{Ce}–\text{O}–\text{Ce})$  mode [77]. The shape of the band at 3478 cm<sup>-1</sup> appeared in both CMO and CYMO as a single band rather than two separate ones as in case of CYO and GDC spectra which is indicative of a certain role of Mn in generating surface modifications upon doping.

Fig. 14(II) elucidates the IR spectra for the samples pre-treated in 30 ppm H<sub>2</sub>S balanced in H<sub>2</sub> at 700 °C for 12 h, then cooled down to room temperature at the same level of H<sub>2</sub>S. The spectrum of each sample shows the same number of bands that detected prior sulfur exposure with more additional and pronounced band manifests at 1346 cm<sup>-1</sup>. This band could be attributed to a partial transformation of sulfite into sulfate [78]. S–H stretching vibration at the wavenumber 2600–2550 cm<sup>-1</sup> was found to be absent in our H<sub>2</sub>S treated samples [79]. It is worth to mention that a peak at 1362 cm<sup>-1</sup> was observed in the diffuse reflectance FTIR for Pd/CeO<sub>2</sub> catalyst and was assigned to adsorbed SO<sub>2</sub> [80]. In addition, previous investigation [76] of the catalytic activity of CeO<sub>2</sub> and various metal oxides has shown that CeO<sub>2</sub> has higher tendency to absorb sulfur when it was treated with H<sub>2</sub>S balanced in He at 623 K.

The concurrent increase in the intensity of the band around 3500 cm<sup>-1</sup> was also correlated to stretching mode of (O–H) bound to metal site on the surface of CeO<sub>2</sub> [81]. Our assumption is that H<sub>2</sub>S undergo dissociation after adsorption on the surface of CeO<sub>2</sub> resulting in formation of H<sub>2</sub>S  $\leftrightarrow$  2H<sup>+</sup> + S<sup>2-</sup>. Liberated H atoms coordinated with surface oxygen and form more hydroxyl groups which accounted for the large increase in the intensity of the bands



**Fig. 13.** SEM images of cross section area of Au coated pellets prepared via conventional solid state synthesis route after conductivity measurement under dry 30 ppm H<sub>2</sub>S in H<sub>2</sub> at 300–800 °C for (i) 10% CYO, (ii) 10% GDC, (iii) 10% CYMO, and (iv) 10% CMO. Au is a current collector. The inset figures represent the SEM profile for the morphology of the surface of the as-prepared pellets. The average elemental analysis presented in different microstructure was determined from the EDX analysis.



**Fig. 14.** FTIR transmittance spectra (4000–500 cm<sup>−1</sup>) measured at room temperature for a homogenous mixture of dried KBr and polycrystalline samples of (a) Ce<sub>0.9</sub>Y<sub>0.1</sub>O<sub>2−δ</sub>, (b) Ce<sub>0.9</sub>Mn<sub>0.1</sub>O<sub>2−δ</sub>, (c) Ce<sub>0.8</sub>Y<sub>0.1</sub>Mn<sub>0.1</sub>O<sub>2−δ</sub> and (d) Ce<sub>0.9</sub>Gd<sub>0.1</sub>O<sub>2−δ</sub>, after (I) sintering in air at 1400 °C for 12h, and (II) samples post-treated in 30 ppm H<sub>2</sub>S in H<sub>2</sub> at 300–800 °C for 48 h.

at 3500 cm<sup>−1</sup> and 1500 cm<sup>−1</sup>. At the same time S<sup>2−</sup> interact with surface oxygen and form SO<sup>2−</sup> which was experimentally identified in MgO [82]. Reduction of CeO<sub>2</sub> resulted in oxygen removal and formation of porous structure which is a facile route for sulfur diffusion into the bulk lattice of CeO<sub>2</sub>. The band concomitant to the formation of sulfates with ν(S=O) vibration mode has been reported to be centered at 1400–1350 cm<sup>−1</sup>, which support our hypothesis. No clear evidences were observed on the formation of Ce<sub>2</sub>O<sub>2</sub>S under the operated conditions. It was instructive to check the validity of our assumption through investigating the reported phase diagram done in the temperature range 63–1073 K. It is suggested that in order to form Ce<sub>2</sub>O<sub>2</sub>S, it requires a higher sulfur partial pressure relative to oxygen partial pressure than used in this study [83].

#### 4. Conclusions

The most important findings in this work could be summarized as:

- PXRD patterns showed that all the prepared samples of Mn-doped CYMO ( $x = 0$ –15 mol%) have maintained the fluorite structure; however, an impurity phase Mn<sub>3</sub>O<sub>4</sub> was detected in small percentage. SEM study has confirmed that Mn doping is influential in enhancing the densification of Y-doped CeO<sub>2</sub> at lower temperatures.
- Doubly doped Ce<sub>0.8</sub>Y<sub>0.1</sub>Mn<sub>0.1</sub>O<sub>2−δ</sub> (CYMO) prepared via solid-state oxide route showed the highest total conductivity of  $\sim 0.061$  S cm<sup>−1</sup> and 0.15 S cm<sup>−1</sup> at 700 °C in air and H<sub>2</sub>, respectively. The higher conductivity of CYMO and CMO under H<sub>2</sub>S (in H<sub>2</sub>) at lower temperatures is explained by the ability of these materials to tolerate the sulfur poisoning and formation of certain types of sulfur contained compounds is expected to be responsible for high conductivity.
- Thermal analysis has shown the effect of Y to impede the reduction of CeO<sub>2</sub> under reducing conditions, while Mn-doped CeO<sub>2</sub> shows a better reducibility. Addition of Mn in presence of Y has a marginal effect on the reduction temperature of CYO. HT-PXRD (RT–800 °C) proved the ability of CeO<sub>2</sub> to maintain the fluorite structural features under reducing atmosphere. After addressing the surface structure through IR and DRS, it is safe to state that Mn oxide species are covering the surface of the doped samples and the presence of surface sulfates was confirmed on the investigated samples.

#### Acknowledgments

This research was supported through funding to the NSERC Solid Oxide Fuel Cell Canada Strategic Research Network from the Natural Science and Engineering Research Council (NSERC) and other sponsors listed at [www.sofccanada.com](http://www.sofccanada.com). Authors also would like to thank the NSERC for funding through the Research Tools and Instruments and Infrastructure grants (RTI) (cat. 1) and the Canada Foundation for Innovation (CFI) for their financial support. One of us (H. H.) would like to thank the Arab Republic of Egypt Fellowship program for providing a scholarship for higher education. Authors also thank Professor Todd Sutherland, Department of Chemistry, University of Calgary, for access to his FTIR instrument.

#### References

- [1] H. Tu, U. Stimming, J. Power Sources 127 (2004) 284.
- [2] T.H. Etzell, S.N. Flengas, Chem. Rev. 70 (1970) 339.
- [3] B.C.H. Steele, Sci. Ceram. 10 (1980) 1.
- [4] R.S. Torrens, N.M. Sammes, G.A. Tompsett, Solid State Ion. 111 (1998) 9.
- [5] T. Zhang, P. Hing, H. Huang, J. Kilner, J. Eur. Ceram. Soc. 22 (2002) 27.
- [6] J. Herring, J. Appl. Phys. 21 (1950) 301.
- [7] J.V. Herle, T. Horita, T. Kawada, N. Sakai, H. Yokokawa, M. Dokuya, Solid State Ion. 86–88 (1996) 1255.
- [8] K. Huang, M. Feng, J.B. Goodenough, J. Am. Ceram. Soc. 81 (1998) 357.
- [9] M.P. Pechini, US Patent 3,330,687, 1967.
- [10] M. Mogensen, T. Lindegaard, U.R. Hansen, G. Mogensen, J. Electrochem. Soc. 141 (1994) 2122.
- [11] J.R. Jurado, J. Mater. Sci. 36 (2001) 1133.
- [12] Y. Zhou, M.N. Rahaman, Acta Mater. 45 (1997) 3635.
- [13] D.P. Fagg, A.L. Shaula, V.V. Kharton, J.R. Frade, J. Membr. Sci. 299 (2007) 1.
- [14] E.L. Santos, R. Muccillo, E.N.S. Muccillo, Mater. Sci. Forum 591–593 (2008) 639.
- [15] Z. Tianshu, P. Hing, H. Huang, J. Kilner, Mater. Sci. Eng. B83 (2001) 235.
- [16] D.P. Fagg, J.C.C. Abrantes, D. Perez-coll, P. Nunez, V.V. Kharton, J.R. Frade, Electrochim. Acta 48 (2003) 1023.
- [17] S. Park, H. Yoo, Solid State Ion. 76 (2005) 1485.
- [18] P.L. Chen, I.W. Chen, J. Am. Ceram. Soc. 76 (1993) 1577.
- [19] S.J. Hong, A.V. Virkar, J. Am. Ceram. Soc. 78 (1995) 433.
- [20] D. Kim, J. Am. Ceram. Soc. 72 (1989) 1415.
- [21] R.D. Shannon, Acta Crystallogr. A32 (1976) 751.
- [22] H.-C. Yao, Y.-X. Zhang, J.-J. Liu, J.-S. Wang, Z.-J. Li, Mater. Res. Bull. 46 (2011) 75.
- [23] S. Lubke, H.-D. Wiemhofer, Solid State Ion. 117 (1999) 229.
- [24] M.C. Pearce, V. Thangadurai, Asia Pac. J. Chem. Eng. 4 (2009) 33.
- [25] H.-C. Yao, X.-L. Zhao, X. Chen, J.-C. Wang, Q.-Q. Ge, J.-S. Wang, Z.-J. Li, J. Power Sources 205 (2012) 180.
- [26] K. Dikmen, J. Alloys Compd. 491 (2010) 106.
- [27] S. Dikmen, H. Aslanbay, E. Dikmen, O. Sahin, J. Power Sources 195 (2010) 2488.
- [28] M. Yashima, S. Kobayashi, T. Yasui, Faraday Discuss. 134 (2007) 369.
- [29] B.C.H. Steele, Solid State Ion. 129 (2000) 95.
- [30] J.A. Kilner, C.D. Waters, Solid State Ion. 6 (1982) 253.
- [31] H. Yapiro, K. Eguchi, H. Arai, Solid State Ionics 36 (1989) 71.

[32] H. Yahiro, Y. Eguchi, K. Eguchi, H. Arai, *J. App. Electrochem.* 18 (1988) 527.

[33] A.B. Kehoe, D.O. Scanlon, G.W. Watson, *Chem. Mater.* 23 (2011) 4464.

[34] D.P. Fagg, S. Garcia-Martin, V. Kharton, J.R. Frade, *Chem. Mater.* 21 (2009) 381.

[35] T.S. Zhang, J. Ma, S.H. Chan, J.A. Kilner, *J. Electrochem. Soc.* 151 (2004) J84.

[36] CH.Y. Kang, H. Kusaba, H. Yahiro, K. Sasaki, Y. Teraoka, *Solid State Ion.* 177 (2006) 1799.

[37] A. Gupta, U.V. Waghmare, M.S. Hegde, *Chem. Mater.* 22 (2010) 5184.

[38] H. Xu, H. Yan, Z. Chen, *J. Power Sources* 163 (2006) 409.

[39] J. Van Herle, T. Horita, T. Kawada, N. Sakai, H. Yokokawa, M. Dokiya, *J. Am. Ceram. Soc.* 80 (1997) 933.

[40] S.K. Tadokoro, T.C. Porfirio, R. Muccillo, E.N.S. Muccillo, *J. Power Sources* 130 (2004) 15.

[41] C. Kleinlogel, L.J. Gauckler, *J. Electroceram.* 5 (2000) 23.

[42] O.S. Polezhaeva, N.V. Yaroshinskaya, V.K. Ivanov, *Inorg. Mater.* 44 (2008) 51.

[43] E.Y. Pikalova, A.N. Demina, A.K. Demin, A.A. Murashkina, V.E. Sopernikov, N.O. Esina, *Inorg. Mater.* 43 (2007) 735.

[44] V. Buscaglia, M.T. Buscaglia, L. Giordano, A. Martinelli, M. Viviani, C. Bottino, *Solid State Ion.* 146 (2002) 257.

[45] P. Patsalas, S. Logothetidis, L. Sygellou, S. Kennou, *Phys. Rev. B* 68 (2003) 035104.

[46] G.R. Bamwenda, H. Arakawa, *J. Mol. Catal. A Chem.* 161 (2000) 105.

[47] F. Chevire, F. Munoz, C.F. Baker, F. Tessier, O. Larcher, S. Boujday, C. Colbeau-Justin, R. Marchand, *J. Solid State Chem.* 179 (2006) 3184.

[48] Q. Li, V. Thangadurai, *J. Chem. Mater.* 20 (2010) 7970.

[49] S.R. Bishop, T.S. Stefanik, H.L. Tuller, *Phys. Chem. Chem. Phys.* 13 (2011) 10165.

[50] A. Corma, P. Atienzari, H. Garcia, J.-Y. Chane-Ching, *Nat. Mater.* 3 (2004) 394.

[51] M. Guo, J. Lu, Y. Wu, Y. Wang, M. Luo, *Langmuir* 27 (2011) 3872.

[52] B. Preetha, C. Janardanan, *Res. J. Recent Sci.* 1 (2012) 85.

[53] V. Butler, C.R.A. Catlow, B.E.F. Fender, J.H. Harding, *Solid State Ion.* 8 (1983) 109.

[54] J.A. Kilner, R.J. Brook, *Solid State Ion.* 6 (1982) 237.

[55] D. Perez-Coll, P. Nunez, J.C.C. Abrantes, D.P. Fagg, V.V. Kharton, J.R. Frade, *Solid State Ion.* 176 (2005) 2799.

[56] J.A. Kilner, *Solid State Ion.* 129 (2000) 13.

[57] A. Tschope, E. Sommer, R. Birringer, *Solid State Ion.* 139 (2001) 255.

[58] X. Guo, R. Waser, *Prog. Mater. Sci.* 51 (2006) 151.

[59] S. Kim, J. Maier, *J. Electrochem. Soc.* 149 (2002) J73.

[60] J. Maier, *Ber. Bunsenges. Physik. Chem.* 90 (1986) 26.

[61] S. Kim, J. Maier, *J. Eur. Ceram. Soc.* 24 (2004) 1919.

[62] T.S. Zhang, J. Ma, Y.J. Leng, S.H. Chan, P. Hing, J.A. Kilner, *Solid State Ion.* 168 (2004) 187.

[63] R.R. Kondakindi, K. Karan, *Mater. Chem. Phys.* 115 (2009) 728.

[64] W. Zajac, J. Molenda, *Solid State Ion.* 192 (2011) 163.

[65] S.R. Bishop, H.L. Tuller, Y. Kuru, B. Yildiz, *J. Eur. Ceram. Soc.* 31 (2011) 2351.

[66] H. Ullmann, N. Trofimienko, F. Tietz, D. Stover, A. Ahmed-Khanbu, *Solid State Ion.* 138 (2000) 79.

[67] T. Hisashige, Y. Yamamura, T. Tsuji, *J. Alloys Compd.* 408 (2006) 1153.

[68] A.J. Jacobson, *Chem. Mater.* 22 (2010) 660.

[69] S.V. Chavan, A.K. Tyagi, *Mater. Sci. Eng. A* 404 (2005) 57.

[70] S.V. Chavan, M.D. Mathews, A.K. Tyagi, *J. Am. Ceram. Soc.* 87 (2004) 1977.

[71] T.H. Nielsen, M.H. Leipold, *J. Am. Ceram. Soc. Discuss. Notes* 47 (1964) 256.

[72] H. He, R.J. Gorte, J.M. Vohs, *Electrochem. Solid-State Lett.* 8 (2005) A279.

[73] D.H. Kim, J.H. Kwak, J. Szanyi, X. Wang, G. Li, J.C. Hanson, C.H.F. Peden, *J. Phys. Chem. C* 113 (2009) 21123.

[74] V.A. Sadykov, T.G. Kuznetsova, G.M. Alikina, Y.V. Frolova, A.I. Lukashhevich, Y.V. Potapova, V.S. Muzykantov, V.A. Rogov, V.V. Kriventsov, D.I. Kochubei, *Catal. Today* 93–95 (2004) 45.

[75] A. Laachir, V. Perrichon, A. Badri, J. Lamotte, E. Catherine, J.C. Lavalley, J. El Fallah, L. Hilaire, F. le Normand, E. Quemere, G.N. Sauvion, O. Touret, *J. Chem. Soc. Faraday Trans.* 87 (1991) 1601.

[76] M. Ziolek, J. Kujawa, O. Saur, J.C. Lavalley, *J. Mol. Catal. A Chem.* 97 (1995) 49.

[77] C. Binet, A. Badri, J.-C. Lavalley, *J. Phys. Chem.* 98 (1994) 6398.

[78] J.C. Lavalley, *Catal. Today* 27 (1996) 377.

[79] J. Coates, *Interpretation of Infrared Spectra, a Practical Approach*, in: R.A. Meyer (Ed.), *Encyclopedia of Analytical Chemistry*, John & Sons Ltd, Chichester, 2000, p. 10815.

[80] T. Luo, J.M. Vohs, R.J. Gorte, *J. Catal.* 210 (2002) 397.

[81] G.J. Pereira, R.H.R. Castro, D.Z. de Floriob, E.N.S. Muccillo, D. Gouve, *Mater. Lett.* 59 (2005) 1195.

[82] Z. Lu, C. Muller, Z. Yang, K. Hermansson, J. Kullgren, *J. Chem. Phys.* 134 (2011) 184703.

[83] R.M. Ferrizz, R.J. Gorte, J.M. Vohs, *Appl. Catal. B Environ.* 43 (2003) 273.